Seismic Vulnerability Assessment of Deteriorated Bridges

FINAL REPORT
February 2021

Submitted By:

Ravi Ranade
Associate Professor

Pinar Okumus
Associate Professor

University at Buffalo
212 Ketter Hall, Buffalo, NY 14260

External Project Managers:

John Picard, PE
Resident Engineer
LaBella Associates, Rochester NY
Former Regional Bridge Maintenance Engineer
New York State DOT - Region 5 (Buffalo)

Bijan Khaleghi, PhD, PE
State Bridge Design Engineer
Washington State DOT

In cooperation with

Rutgers, The State University of New Jersey
And
U.S. Department of Transportation
Federal Highway Administration

Disclaimer Statement

The contents of this report reflect the views of the authors, who are responsible for the facts and the accuracy of the information presented herein. This document is disseminated under the sponsorship of the Department of Transportation, University Transportation Centers Program, in the interest of information exchange. The U.S. Government assumes no liability for the contents or use thereof.

The Center for Advanced Infrastructure and Transportation (CAIT) is a Regional UTC Consortium led by Rutgers, The State University. Members of the consortium are Atlantic Cape Community College, Columbia University, Cornell University, New Jersey Institute of Technology, Polytechnic University of Puerto Rico, Princeton University, Rowan University, SUNY - Farmingdale State College, and SUNY - University at Buffalo. The Center is funded by the U.S. Department of

1. Report No.	2. Government Accession No.	3. Recipient's Catalog No.
CAIT-UTC-REG 29		

4. Title and Subtitle	5. Report Date
Seismic Vulnerability Assessment of Deteriorated Bridges	Feb 22, 2021
	6. Performing Organization Code CAIT/University at Buffalo
7. Author(s) Ravi Ranade https://orcid.org/0000-0001-6030-837; Pinar Okumus https://orcid.org/0000-0002-2197-3261, and Hanmin Wang https://orcid.org/0000-0001-5834-1930	8. Performing Organization Report No. CAIT-UTC-REG 29
9. Performing Organization Name and Address University at Buffalo 212 Ketter Hall, Buffalo, NY 14260	10. Work Unit No.
	11. Contract or Grant No. 69A3551847102
12. Sponsoring Agency Name and Address Center for Advanced Infrastructure and Transportation Rutgers, The State University of New Jersey 100 Brett Road Piscataway, NJ 08854	13. Type of Report and Period Covered Final Report 1/1/2020-12/31/2020
	14. Sponsoring Agency Code

15. Supplementary Notes
U.S. Department of Transportation/OST-R
1200 New Jersey Avenue, SE
Washington, DC 20590-0001

16. Abstract

The seismic vulnerability assessment methods currently used by state DOTs typically rely on as-built conditions of bridges. However, due to environmental deterioration, the structural performance can degrade over time. This research demonstrates the application of a combined durability-fragility assessment framework, developed by the authors, for a group of bridges in the states of New York and Washington. Corrosion of steel reinforcement is the main deterioration mechanism considered for durability evaluation. The computational framework demonstrated in this research consists of three parts: corrosion modeling, seismic fragility analysis, and risk analysis. The results show that all bridges become more vulnerable to seismicity due to corrosion deterioration. For a group of bridges, the order of vulnerability can change over time due to corrosion which affects the fragility each bridge differently depending on its layout, geometry, reinforcement detail, cover thicknesses, axial load ratio, salt exposure, etc. These results can be used to update the vulnerability scores of bridges and prioritize maintenance activities.

17. Key Words	18. Distribution Statement
Seismic resilience; Deterioration; Corrosion rate; Cracking; Fragility; Service life	

19. Security Classification (of this report)	20. Security Classification (of this page)	21. No. of Pages	22. Price
Unclassified	Unclassified	60	

Form DOT F 1700.7 (8-69)

Acknowledgments

This research was financially supported by the Region 2 University Transportation Center, which is funded by the US Department of Transportation and by University at Buffalo (UB), the State University of New York. Financial support was also provided by the Institute of Bridge Engineering at UB. These financial supports are gratefully acknowledged. The opinions, findings and views expressed in this study are the ones of the authors only and do not necessarily reflect the views, policies, standard specifications or regulations of the parties acknowledged above. Funding agencies do not assume any liability for the contents or the use thereof.

Table of contents

List of figures

List of tables

Nomenclature

A_0	Original rebar area
A_1	Area parameter 1 depending on D_0, $P(t)$, θ_1 and b in pitting corrosion model
A_2	Area parameter 2 depending on D_0, $P(t)$, θ_2 and b in pitting corrosion model
$A(t)$	Rebar area at time t
A_R	Ratio of exceedance frequency at a given PGA to the exceedance frequency at a PGA that is 10-times smaller than this PGA
b	Width of the pit area
C	Thickness of concrete cover
$C_{CI}(x,t)$	Chloride concentration at spatial coordinate x and time t
C_s	Chloride content at the outer surface of concrete
D_{CI}	Effective chloride diffusion coefficient
D_0	Original rebar diameter
d	The limiting value of EDP used to define a damage level
E	Elastic modulus of concrete
EDP	Engineering demand parameter
erf(.)	Error function
f_0	Yield strength of non-corroded reinforcement
$f(t)$	Yield strength of corroded rebar at time t
$f_t(t)$	Yield strength of transverse rebar at time t

f'_c	Compressive strength of unconfined concrete
$f_{cc}(t)$	Compressive strength of confined concrete at time t
IM_i	Ground motion intensity measure
$H(a)$	Probability of exceeding of a PGA (a)
K	The ratio of $\lambda(t)_{afcrack}$ to $\lambda(t)_{bfcrack}$
K_H	Slope parameter
M_{loss}	Mass loss of steel per unit length consumed to produce rust
M_r	Mass of rust per unit length of one rebar
m_{loss}	Percent of rebar mass loss (or area loss per unit length) due to corrosion
m	Number of ground motion intensity levels
n_j	Total ground motion records at j^{th} ground motion intensity levels
$P(t)$	Pit depth
P_{corr}	Internal pressure caused by rust expansion
Q_{corr}	Percent weight loss (or area loss) of rebar
R	Pitting factor
r_0	Radius of the thick-wall cylinder (concrete cover)
r_i	Radius of rebar
r	Distance from the center of the thick-wall model to the interface between the rust and concrete
T_1	Time when the peak corrosion rate is reached
t_{cr_lon}	Longitudinal rebar corrosion initiation time
$W(t)$	Crack width of concrete cover at time t
W_{cri}	Critical crack width

$W_{i,i=1,2,3}$	Fitting coefficients
z_j	Number of records which cause a particular damage state in the j[th] IM level
i_{corr}	Current density
β	Parameter of standard normal distribution
$\bar{\beta}$	Estimated parameter of standard normal distribution
δ_0	Thickness of the porous zone
δ_c	Radial displacement caused by rust expansion
ε_{cu}	The maximum compressive strain in the confined concrete
ε_{su}	Strain in transverse rebar at ultimate strength
θ	Parameter of standard normal distribution
$\bar{\theta}$	Estimated parameter of standard normal distribution
θ_1	Angle parameter 1 depending on D_0, $P(t)$, and b in pitting corrosion model
θ_2	Angle parameter 2 depending on D_0, $P(t)$, and b in pitting corrosion model
$\lambda(t)_{corr}$	Corrosion rate in mm/year
$\lambda(t)_{afcrack}$	Corrosion rate at critical crack width
$\lambda(t)_{bfcrack}$	Corrosion rate before cracking
ρ_{long}	Longitudinal reinforcement ratio
ρ_r	Mass density of rust
ρ_s	Mass density of the original (non-corroded) steel
$\rho_{trans}(t)$	Volumetric ratio of transverse rebar at time t

$\Delta A(t)$	Cross-sectional area loss of reinforcement at time t
$\Phi(.)$	Standard normal cumulative distribution function (CDF)
ν	Poisson's ratio of concrete
σ	Circumferential stress caused by rust expansion

Chapter 1: Introduction and Motivation

Reinforced-concrete (RC) highway bridges are susceptible to damage due to earthquakes and other natural hazards. A sudden loss of functionality of a bridge due to an earthquake can cause significant downtime, repair/reconstruction costs, and even loss of life [1-3]. At the same time, the corrosion of steel reinforcement, a common durability problem in highway bridges especially in the northern and coastal US [4, 5], can weaken an RC bridge gradually over time and increase the severity of damage caused by an earthquake relative to the damage to the bridge in its as-built condition [6, 7]. Therefore, a quantitative framework is needed for assessing the time-dependent damage risk to RC bridges under the combined effects of corrosion and earthquakes.

Several studies in the literature have reported the development of such frameworks. These studies can be broadly classified into two categories depending on the corrosion model. The majority of the studies [6-11] assumed uniform corrosion of steel reinforcement, whereas only a few studies considered a more realistic pitting corrosion model [12-15]. While pitting corrosion is more difficult to model compared to the uniform corrosion, the localized pitting corrosion is the most commonly observed corrosion mechanism in real RC bridges under chloride-rich environments [16, 17]. The literature also has examples of these frameworks expanded to consider different failure types [6, 7, 13] and lifetime costs [8].

The aforementioned studies have a few assumptions that limit their application to real RC bridges. The corrosion rate is influenced by cracking of concrete cover [18, 19], however, this influence has been considered only by a few researchers [15]. Overly simplified corrosion

estimates yielded conflicting results in the literature on whether seismic fragility is affected by deterioration [20]. Finally, as the structural capacity changes due to corrosion, the thresholds of engineering demand parameters (e.g., lateral drift), used to define damage states in fragility analysis, also change with time. This effect has been taken into account only by a limited number of studies [10, 12, 14]. In this study, all of the above limitations have been addressed as described in the following sections.

The objective of this research was to develop and demonstrate a computational framework that estimates the risk of seismic damage over the entire service life, accounting for the effects of corrosion, for groups of real RC bridges. Two groups of bridges, owned by the New York State Department of Transportation (NYSDOT) and by Washington State Department of Transportation (WSDOT), were considered in this project. The computational framework consists of three parts: corrosion modeling, seismic fragility analysis, and risk analysis. Each of these parts are described in the next three chapters, followed by the results and discussion and the main conclusions of this project.

Chapter 2: Corrosion Modeling

Chloride-induced corrosion is the focus of this study, as it is the most common cause of bridge degradation in the northern and coastal US. Chloride-induced corrosion occurs in two phases: initiation and propagation. In the initiation phase, chloride ions from the outside environment gradually ingress through the concrete cover to the steel reinforcement surface. Once the chloride ion concentration at the reinforcement surface reaches a critical level, the rebar corrosion initiates, which marks the beginning of the corrosion propagation phase. The cross-sectional areas of the transverse and longitudinal rebars decrease in the propagation phase due to corrosion.

In the following sections (Sections 2.1 and 2.2), the mathematical equations describing the corrosion initiation and propagation processes are given. This is followed by Section 2.3 that presents a summary of the parameter values used for modeling corrosion in the groups of bridges investigated in this project.

2.1 Corrosion initiation

The time to corrosion initiation is typically determined by using the Fick's second law of diffusion, which is a complex partial differential equation. Time to corrosion initiation can be calculated using the Crank's solution [21] given in Equation 1.

$$C_{CI}(x,t) = C_s\left[1 - \text{erf}\left(\frac{x}{2\sqrt{D_{CI}\,t}}\right)\right] \quad (1)$$

2.2 Corrosion propagation

Active corrosion of steel reinforcement happens during the corrosion propagation phase. Corrosion can either occur uniformly throughout a rebar or occur locally due to the formation of a pit [22]. Chloride ion diffusion typically leads to local or pitting corrosion, which is considered in our study. Corrosion products apply a radially outward pressure due to their expansive nature, as their volume is about 3-4 times that of the original steel. However, the start of the corrosion propagation phase does not damage the concrete cover right away, as discussed below.

The corrosion propagation phase can be further divided into four stages. In the first stage, the corrosion products fill the porous zone at the rebar-concrete interface without causing any stress in the surrounding concrete. Once the pores are saturated, in the second stage, the corrosion products start to apply an outward radial pressure causing tensile hoop stress in the surrounding concrete. This process continues until the tensile stress in concrete reaches the concrete tensile strength at which point the cover cracks, marking the end of the second stage. In the third stage, the corrosion rate increases due to an increase in the number of cracks as well as an increase in the widths (openings) of the existing cracks. In the fourth stage, after reaching a certain crack width, the corrosion rate stabilizes as the built-up of corrosion products shield the rebar core from extremely rapid corrosion. All of the aforementioned stages of corrosion are captured in our model, as described below.

2.2.1 Pitting corrosion

During pitting corrosion, a rebar's cross-sectional area will continuously decrease over time. As discussed above, pitting corrosion is typically observed in real RC structures during the corrosion propagation stage. As the name suggests, pitting corrosion creates a pit starting at the surface of the rebar. Unlike uniform corrosion that reduces rebar area throughout the length of the rebar; in pitting corrosion, the rebar mass loss is local as the depth of the pit becomes larger with time. Val and Melchers [23] proposed a hemispherical model to simulate pitting corrosion as shown in Figure 1.

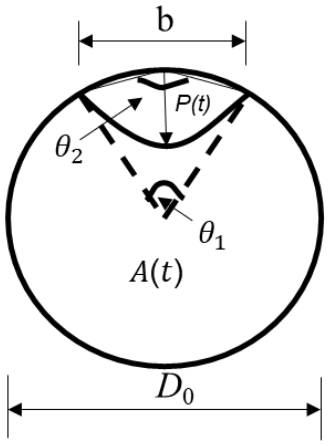

Figure 1: Pitting corrosion shown on rebar cross-section view (adapted from Val and Melchers [23])

The rebar area, A(t), at time t after corrosion initiation can be estimated using Equation 2 [23]:

$$A(t)_{pitting} = \begin{cases} \frac{\pi {D_0}^2}{4} - A_1 - A_2, & P(t) \le D_0 \frac{\sqrt{2}}{2} \\ A_1 - A_2, & D_0 \frac{\sqrt{2}}{2} < P(t) \le D_0 \\ 0, & P(t) > D_0 \end{cases} \quad (2)$$

The parameters A_1 and A_2 can be estimated by the following equations [23]:

$$A_1 = 0.5\left[\theta_1\left(\frac{D_0}{2}\right)^2 - b\left|\frac{D_0}{2} - \frac{P(t)^2}{D_0}\right|\right] \quad (3)$$

$$A_2 = 0.5\left[\theta_2 P(t)^2 - b\frac{P(t)^2}{D_0}\right] \quad (4)$$

$$\theta_1 = 2\arcsin(\frac{b}{D_0}), \theta_2 = 2\arcsin(\frac{b}{2P(t)}) \quad (5)$$

$$b = 2P(t)\sqrt{1 - \left(\frac{P(t)}{D_0}\right)^2} \quad (6)$$

The pitting depth, $P(t)$, is expressed by Equation 7 [23]:

$$P(t) = R\int_{t_{corr}}^{t} \lambda(t)dt \quad (7)$$

where, $\lambda(t)$ is the corrosion rate, expressed as:

$$\lambda(t) = 0.0116 \times i_{corr} \quad (8)$$

In addition to the reduction in rebar area, the stress concentration at the sites of pitting corrosion has been observed to decrease the yield strength (calculated with the reduced rebar area) of the reinforcement [24]. This reduction in yield strength is expressed by Equation 9 [24]:

$$f(t) = (1.0 - 0.005Q_{corr})f_0 \quad (9)$$

where, Q_{corr} is the percent weight loss (or area loss) of rebar expressed as:

$$Q_{corr} = \frac{A_0 - A(t)}{A_0} * 100 \quad (10)$$

2.2.2 Crack initiation time

The buildup of rust causes tensile stress to increase with time in the concrete surrounding the rebar. When this stress reaches the tensile strength of concrete, a crack forms in the concrete cover. Assuming that all the corrosion products remain inside, the rebar mass loss computed below can be converted into internal radial pressure caused by rust expansion using Equations 11, 12 and 13 [25]. Concrete around the rebar is modeled as a thick-walled cylinder, in which the circumferential stress can be calculated using Equation 14. For simplifying the model, the entire cover is assumed to crack instantaneously when the tensile stress in the circumferential direction at the interface between the rust and concrete reaches the tensile strength of the concrete. As the rebar mass loss (m_{loss}) is a function of time, crack initiation time can be calculated using these equations.

$$m_{loss} = Q_{corr} \times unit\ thickness\ of\ section\ (1\ mm) \tag{11}$$

$$P_{corr} = \frac{m_{loss} E D_0}{90.9(1+\nu+\psi)(D+2\delta_0)} - \frac{2\delta_0 E}{(1+\nu+\psi)(D_0+2\delta_0)} \tag{12}$$

$$\psi = \frac{{D_0}^2}{2C(C+D_0)} \tag{13}$$

$$\sigma = \frac{P_{corr} {r_i}^2}{{r_0}^2 - {r_i}^2}\left[1 + \frac{{r_0}^2}{r^2}\right] \tag{14}$$

2.2.3 Time-dependent crack width

After crack initiation, crack width gradually increases with time. For concrete, Equation 15 [26] is used to capture the change in crack width with time:

$$W(t) = 0.0575\ (\Delta A(t) - \Delta A(t_{cr})) \tag{15}$$

2.2.4 Corrosion rate

Previous studies [19, 27] have shown that the existence of cracks in concrete increases the corrosion rate significantly, depending on the crack width. This is because cracks in the cover provide an easier ingress path for water, oxygen, and chloride ions. As explained above, corrosion propagation can be divided into four stages. In stages 1 and 2, the corrosion rate is constant prior to crack initiation. In stage 3, after cracking of the concrete cover, corrosion rate increases with an increase in the number and widths of the cover cracks. Due to the lack of experimental data and for simplifying the numerical analysis, the corrosion rate is assumed to increase linearly with time in our study. In stage 4, corrosion rate reaches a peak value and remains constant thereafter, when the cover crack width reaches a critical value that depends on the material.

The time when the critical crack width is reached is iteratively determined using the following steps:

1. Assume a a linear increase of the corrosion rate ($d\lambda/dt$) with time to calculate the time-dependent corrosion rate [$\lambda(t)$] after crack initiation.
2. Calculate the time T_1 when the corrosion rate reaches its peak value for a given material and determine the corresponding rebar area loss at T_1.
3. Calculate the crack width at T_1 using the relation between rebar mass loss and crack width of the material, as discussed in Section: *Time-dependent crack width.*
4. Check if the crack width reaches the critical crack width for the material at T_1. If it does, the assumed $d\lambda/dt$ and the corresponding time T_1 are correct; else, vary $d\lambda/dt$ and start again from step 1 until this check is satisfied.

2.3 Parameters used in corrosion modeling

Corrosion initiation phase: In this study, all the bridges were analyzed from the time of original construction, and therefore, the initial unbound chloride concentration in the cover concrete of all the bridges was assumed zero. The surface chloride concentration (C_s) was assumed to be 8.6 kg/m^3 and 3.6 kg/m^3 for bridges from NYSDOT and WSDOT, respectively, which represents the exposure environment created by the de-icing salts, based on Weyers et al. [28]. The chloride diffusion coefficient (D_{CI}) was assumed to be 2.6×10^{-12} m^2/s for bridges from NYSDOT [28]. Due to the lack of reliable corrosion data for Washington State, the chloride diffusion coefficient (D_{CI}) was assumed to be 4.3×10^{-12} m^2/s, based on available field tests of bridge beams in USA [29]. The critical chloride content for corrosion initiation at the rebar-concrete interface was assumed to be 1.2 kg/m^3 [30].

Corrosion rate: A corrosion rate of 0.0116 mm/year suggested in the literature [31] was assumed prior to crack initiation. Due to the lack of peak corrosion rate data in real bridges, the peak corrosion rate after crack initiation was assumed two times (equal to 0.0232 mm/year) that of the corrosion rate before crack initiation. It was also assumed that no repair was performed during the bridge's service life. The critical crack width beyond which the corrosion rate became constant was assumed to be 0.2 mm [15]. Table 1 summarizes all the parameters used in the corrosion model.

Table 1: Parameters used in corrosion model

Parameters	NYSDOT	WSDOT	Source
C_s (kg/m^3)	8.6	3.6	[28]
D_{CI} (m^2/s)	2.6×10^{-12}	4.3×10^{-12}	[28, 29]
Critical chloride content at rebar surface (kg/m^3)	1.2	1.2	[30]
$\lambda(t)_{bfcrack}$ (mm/year)	0.0116	0.0116	[31]
$\lambda(t)_{afcrack}$(mm/year)	0.0232	0.0232	As explained in section 2.3
Critical crack width, W_{cri} (mm)	0.2	0.2	Cui et al. (2018)
ν	0.18	0.18	[25]
δ_0 (mm)	20×10^{-3}	20×10^{-3}	
R	6	6	[23]

2.4. Outcomes of corrosion modeling

The outcome of the corrosion model is the estimation of loss of reinforcement area due to corrosion for bridge piers at 0 years, 25 years, 50 years and 75 years along their life-span. Both longitudinal and transverse reinforcement in piers were considered.

Chapter 3: Seismic Fragility Analysis

A seismic fragility curve provides the probability of a structure exceeding a specified level of damage as a function of a ground motion intensity measure (*IM*), such as peak ground acceleration (PGA). A seismic fragility curve is commonly modeled by a lognormal cumulative distribution function, as shown in Equation 16. In this study, the engineering demand parameter (EDP) was displacement ductility. The distribution parameters (θ and β) of the lognormal cumulative distribution function were estimated from the statistical analysis of the results of an incremented dynamic analysis.

$$P(EDP \geq d \mid IM = IM_i) = \Phi\left[\frac{ln(IM_i) - \ln(\theta)}{\beta}\right] \quad (16)$$

3.1. Steps of seismic fragility analysis

The fragility curves in this study were developed through the six steps summarized below.

Step 1: Ground motion selections

A far-field ground motion record set, including 44 records provided by FEMA P695 [32], was used. The PGA was used as the earthquake intensity measure. All ground motion records used in this study were scaled linearly from 0.1g to 2.0g with increments of 0.1g. It should be noted that the ground motions recommended by FEMA P695 are for the risk analysis of structures in the western U.S. Due to the low seismicity in New York State, there are no ground motion records for New York State. Therefore, ground motion records from FEMA P695 were also used in the risk analysis of NYSDOT bridges due to their reliability and wide recognition in risk assessments.

Step 2: Structural model

Finite element models of bridge elements (i.e., pier columns or pier walls) were created in an open-source finite element software, OpenSEES [33]. The piers were simulated using four degree of freedom, fiber-based, displacement beam-column elements. The superstructure and other bridge elements were represented as point masses, but they were otherwise excluded from the model for computational efficiency. Additional details of the finite element model are provided in Section 5.2.

Step 3: Incremented dynamic analysis

Incremented dynamic analysis (IDA) proposed by Vamvatsikos and Cornell [34] was performed in this study. It involved a large number of nonlinear response history analyses using ground motions that were scaled systematically to increasing earthquake intensities (PGA) until a given damage level was achieved. The resulting structural response data was statistically analyzed to determine the fragility curve for that damage level.

Step 4: Time-dependent damage states and damage index

The level of damage is typically characterized by discrete damage states defined by certain thresholds of a *damage measure*. Corrosion affects the structural capacity, and therefore, these thresholds should change with time. In this study, *displacement ductility* was used as the damage measure, which is defined as the ratio of the peak lateral displacement (obtained from the dynamic analysis) to the yield displacement, both of which change due to the effects of corrosion. The yield displacement, obtained from a push-over analysis, is defined as the lateral displacement

corresponding to the yielding of the outermost longitudinal rebar under tension. Based on the above definitions, four damage states are defined as follows:

1. Slight Damage: Slight damage is assumed to occur when the peak lateral displacement is equal to the yield displacement. At this level, the concrete cover is assumed to have visible cracks under earthquake load near the maximum moment locations.
2. Moderate Damage: Moderate damage is assumed to occur when the maximum compressive strain in the concrete core (confined by steel reinforcement) at the column base reaches 0.002 [14]. At this strain, concrete cover near the bottom of a bridge column is assumed to have minor spalling.
3. Extensive Damage: Extensive damage is defined when the column reaches the displacement ductility that is equal to the geometric mean of the displacement ductility corresponding to the moderate damage state and the complete damage state, similar to other studies [14].
4. Complete damage: Complete damage is defined to occur when the maximum compressive strain in the confined concrete reaches ε_{cu} calculated in Equation 17 [35]. This value of strain in concrete corresponds to the fracture of the first transverse tie [12, 14].

$$\varepsilon_{cu} = 0.004 + \frac{1.4\rho_s f_t(t)\varepsilon_{su}}{f_{cc}(t)} \tag{17}$$

Step 5: Estimation of the parameters of fragility functions

The parameters of the fragility functions can be obtained using several methods [36]. In this study, the maximum likelihood method [37] was used to estimate the parameters of the fragility curves using the expression given below:

$$\{\bar{\theta},\bar{\beta}\} = argmax \sum_{j=1}^{m} \left\{ ln\binom{n_j}{z_j} + z_j ln\Phi\left(\frac{ln(IM_i)-\theta}{\beta}\right) + (n_j - z_j) ln\left[1-\Phi\left(\frac{ln(IM_i)-\theta}{\beta}\right)\right]\right\} \quad (18)$$

Step 6: Development of continuous fragility curves

Due to the high computational cost of IDA, the fragility curves were computed in this study only for four time points along a bridge's service life: 0 years, 25 years, 50 years, and 75 years since the original construction of a given bridge. As explained above, each fragility curve is described by the lognormal distribution parameters θ and β. Two different second-order polynomials as expressed by Equation 19 were fitted through the four values of θ and β using the nonlinear least square method to compute the coefficients W_1, W_2 and W_3, similar to other studies [11]. Here, $Para(t)$ is either θ or β as a function of time t.

$$Para(t) = W_1 \times t^2 + W_2 \times t + W_3 \quad (19)$$

3.2. Outcomes of seismic fragility analysis

The outcome of seismic fragility analysis is seismic fragility functions at 0 years, 25 years, 50 years and 75 years along the service life of a bridge. Outputs of the corrosion model (loss of reinforcing bar area) are used as input to the seismic fragility analyses to understand seismic damage probability considering corrosion.

Chapter 4: Integration of Seismic Hazard and Fragility Curves

While a fragility function quantifies the probability of damage to a structure exposed to a given set of ground motions, it does not account for the probability of the hazard. Seismic hazard curves are used for this purpose [38], which provide the annual probability of exceeding a certain ground motion intensity. Obtaining a seismic hazard curve was particularly important for this research project, due to differences in seismic risk in New York and Washington and the lower intensity of ground motions expected in New York. Figure 2 shows a typical seismic hazard curve in which the annual probability of exceedance and PGA (an intensity measure) are plotted on log scales.

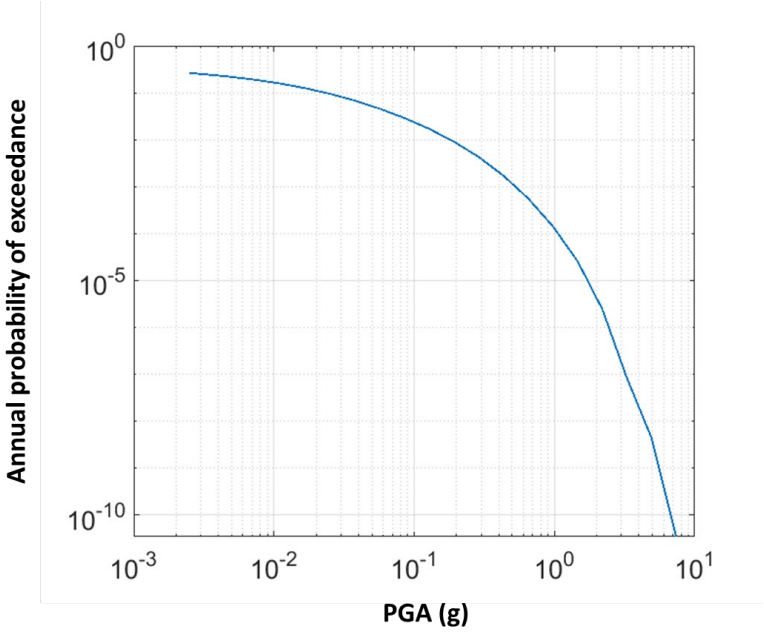

Figure 2: A typical seismic hazard curve

4.1 Method to generate seismic hazard curves

Seismic hazard curves can be generated by both deterministic and probabilistic methods. In this study, probabilistic seismic hazard analysis (PSHA) [39] is used, which considers the uncertainty in the location, size, and resulting shaking intensity of earthquakes incorporating the historical data of a region. Seismic hazard curves were generated using the Unified Hazard Tool [38] provided by the United States Geological Survey (USGS). The hazard curve provided by the tool shows the annual frequency of exceeding a given PGA (at a given location) plotted against the PGA, which can be converted to the probability of exceeding that PGA using the Poisson distribution.

4.2 Method to integrate seismic hazard curves and fragility curves

ASCE 43-05 [40] provides a method to calculate the probability of exceeding a given damage state considering both the seismic hazard curve and the fragility curve for that damage state. In this approach, the seismic hazard curve is modeled by an approximate equation, as shown below:

$$H(a) = K_I \times a^{-K_H} \tag{20}$$

where $H(a)$ is the probability of exceeding of a PGA (a). K_I is a constant, and K_H is a slope parameter defined by :

$$K_H = \frac{1}{\log(A_R)} \tag{21}$$

where A_R is the ratio of exceedance frequency at a given PGA to the exceedance frequency at a PGA that is 10-times smaller than this PGA. The probability of exceeding a given damage state is obtained by convolution of the seismic hazard curve and fragility curve, which is expressed by:

$$P_i = \int_0^{+\infty} H(a) \times \frac{dF_c}{da} da \tag{22}$$

where P_i is the probability of exceeding a damage state i, $\frac{dF_c}{da}$ is the log-normal probability density function, which is the derivative of fragility curve (F_c) with respect to the PGA (a). Using Equation 20 and Equation 21 along with Equation 22, P_i can be expressed analytically as shown below, where θ and β are parameters of the lognormal distribution representing the fragility curve for a given damage state.

$$P_i = H(\theta) \times \exp[(K_H\beta)^2/2] \tag{23}$$

4.3. Outcomes of integration of seismic hazard and fragility curves

The outcome of this process is the probability of exceedance of a given damage state as a function of PGA, considering both the hazard curve and the fragility curve. For each bridge, the seismic hazard curve generated by USGS was first converted to the analytical form in Equation 20 using the nonlinear least square fitting method, as shown for one of the bridges in Figure 3. The fragility curve was developed for a given damage state using the steps given in Chapter 3. Then, the damage probability for that damage state was obtained using Equation 23.

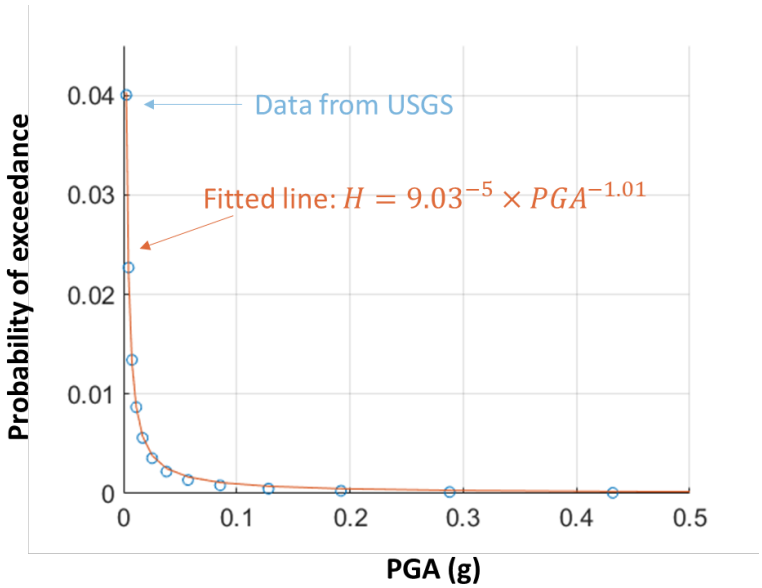

Figure 3: Bridge NY-1 seismic hazard function

Chapter 5: Bridge Details and Modeling Strategies

This chapter provides a detailed description of the analyzed bridges and the modeling strategies adopted in this study. Sixteen bridges were selected in total, 8 from NYSDOT and 8 from WSDOT. All the bridges were built between 1960 and 1990 with RC substructures. In the following sections, the details of the bridges from NYSDOT and WSDOT are given. Then the modeling strategies are discussed, including: 1) material model for concrete and rebar, 2) finite element model, including element choices and boundary conditions.

5.1 Bridge details

Details of the bridges from NYSDOT are summarized in Table 2, including built year, number of spans, span lengths, types of superstructure and substructure, sizes of rebars, design compressive strength of concrete, and yield strength of rebars. The layouts of the 8 NYSDOT bridge substructures are shown in Figure 4. Similarly, the details for WSDOT bridges are summarized in Table 3 and their layouts are given in Figure 5. It should be noted that the bridges from WSDOT were expanded to carry more lanes after the original construction, but only the original design information was available for this study. Therefore, the layouts of WSDOT bridge substructures are based on the original designs.

Table 2: Summary of NYSDOT bridges

Bridge	Built year	Spans	Span length (m)		Superstructure		Substructure				
			Side	Middle	Deck type	Girder type	Substructure type	Rebar Size*		Concrete strength (MPa)	Rebar strength (MPa)
								Longitudinal	Transverse		
NY-1	1990	3	23.0	23.0	Concrete	Steel	Column	No.32	No.13	21	276
NY-2	1970	3	29.0	38.0	Concrete	Steel	Wall	No.19, No.22	No.16	21	276
NY-3	1962	3	26.0	48.0	Concrete	Steel	Columns	No.25	No.13	21	276
NY-4	1983	3	24.0	34.0	Concrete	Steel	Wall	No.32	No.13	21	276
NY-5	1970	2	27.8	-	Concrete	Steel	Columns	No.36	No.16	21	276
NY-6	1972	2	27.4	-	Concrete	Prestressed concrete	Wall	No.16	No.16	21	276
NY-7	1985	2	34.4	-	Concrete	Steel	Wall	No.16	No.16	21	276
NY-8	1973	3	38.1	-	Concrete	Steel	Wall	No.19	No.16	21	276

*The numbers indicate rebar diameter in mm.

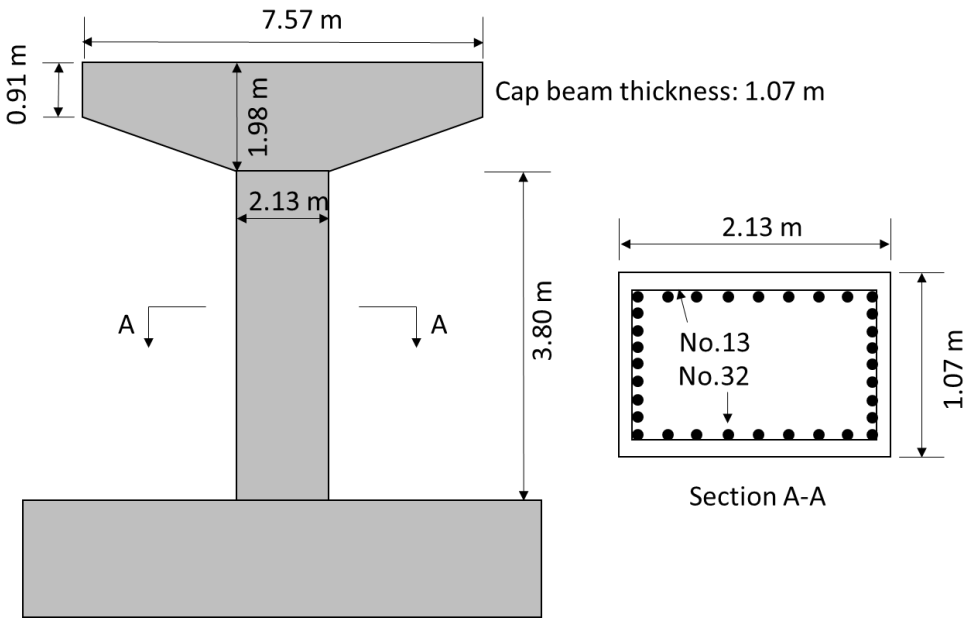

(a) Bridge NY-1

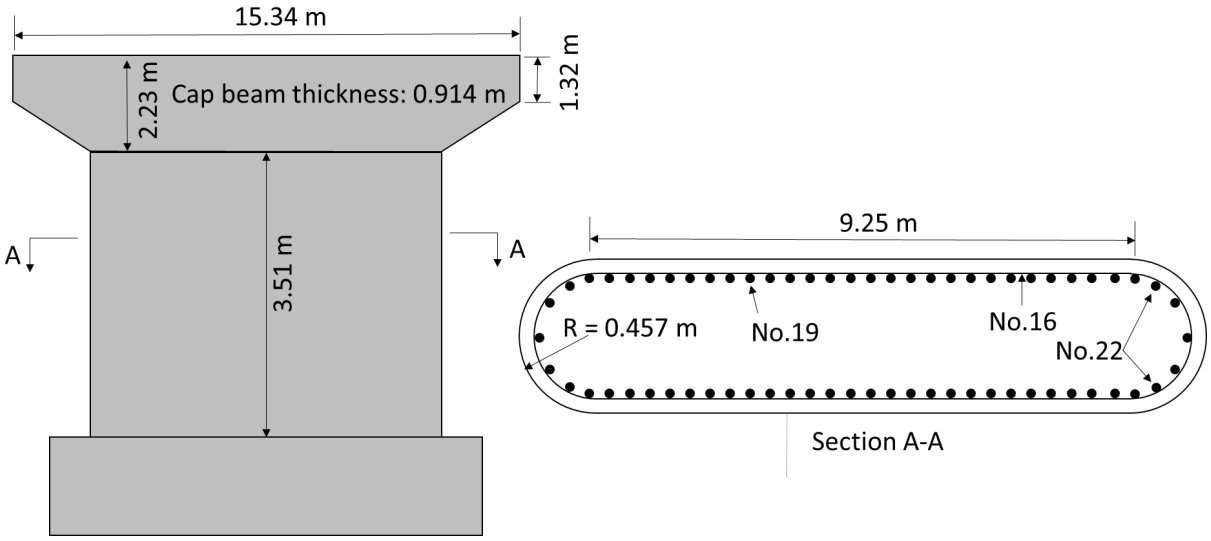

(b) Bridge NY-2

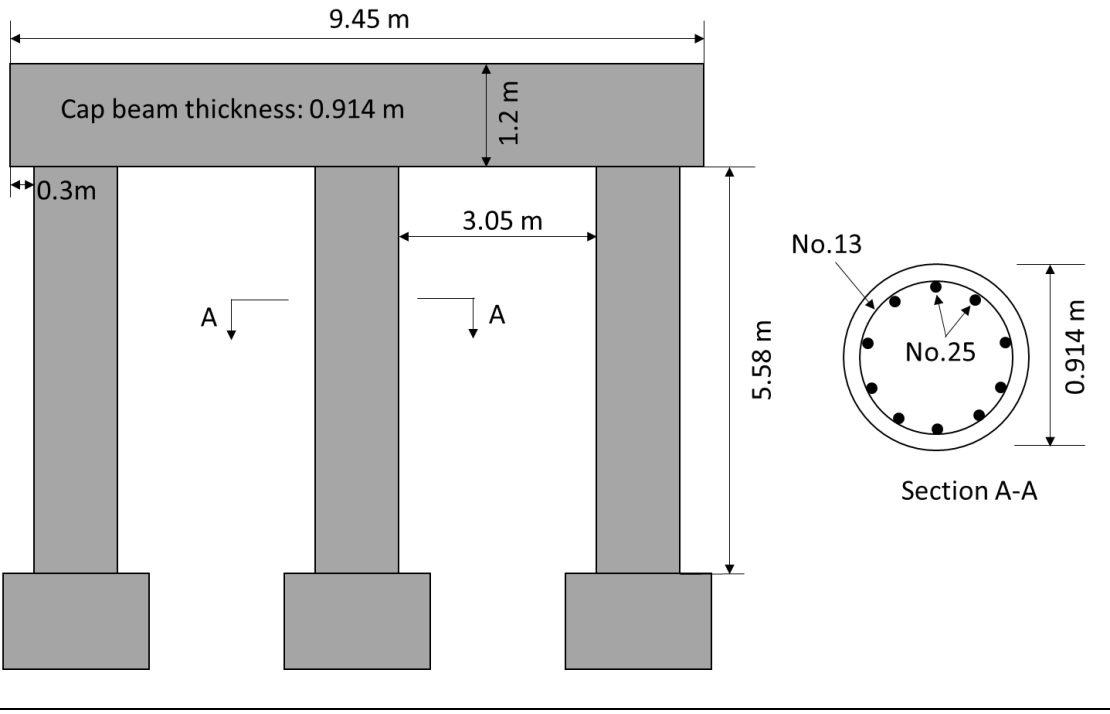

(c) Bridge NY-3

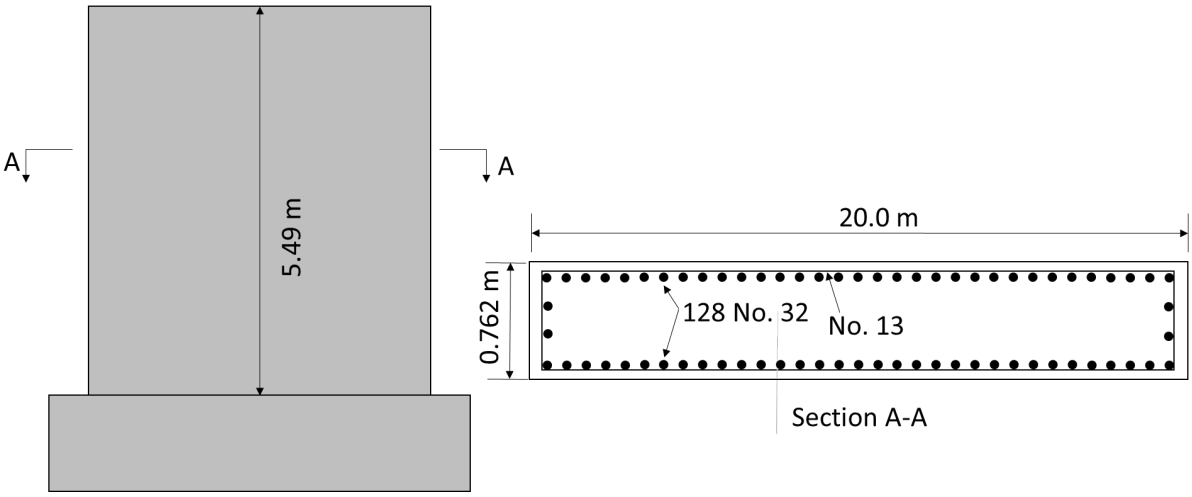

(d) Bridge NY-4

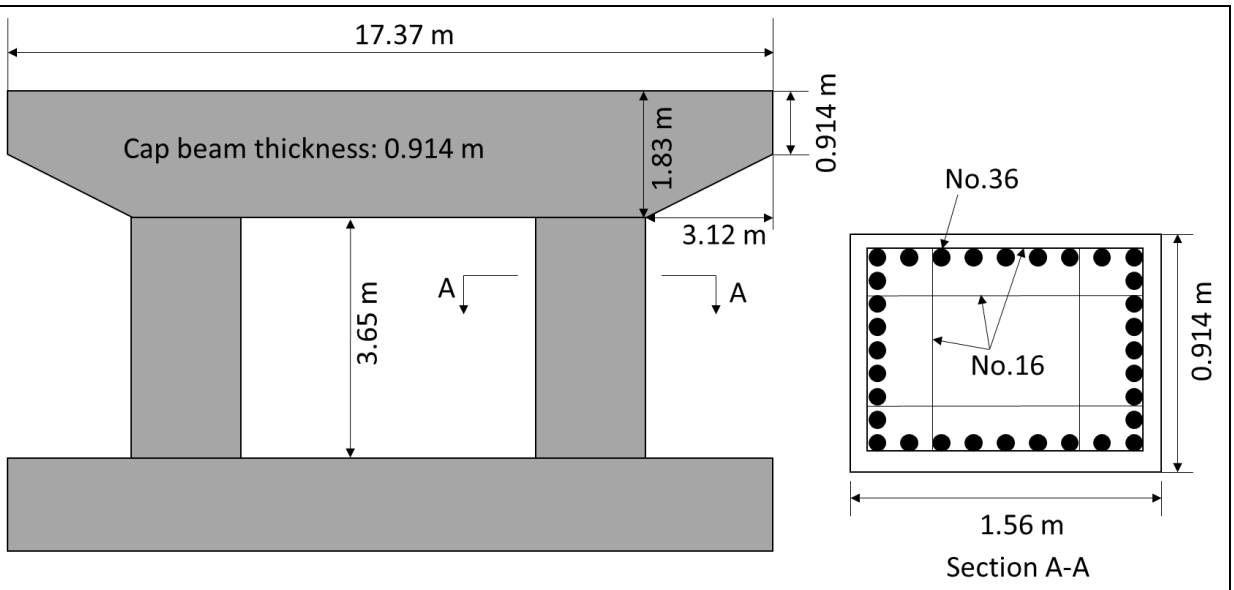

(e) Bridge NY-5

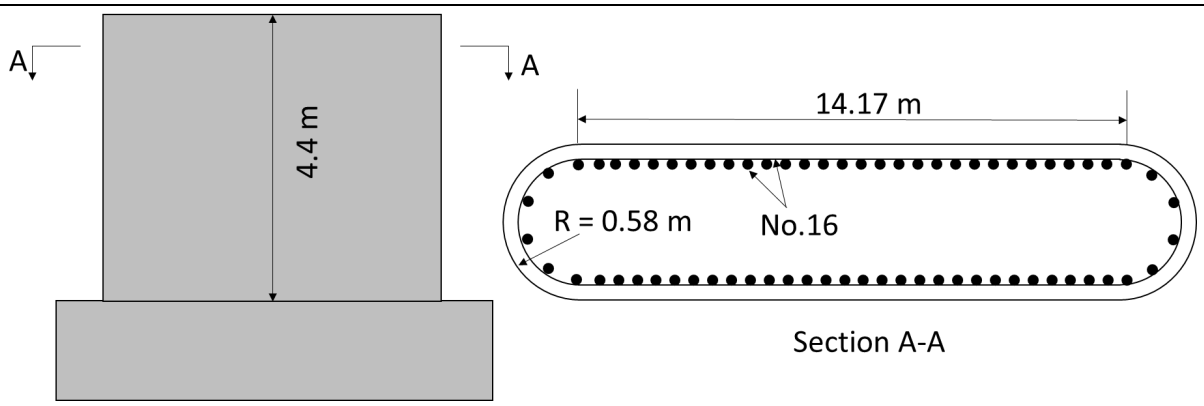

(f) Bridge NY-6

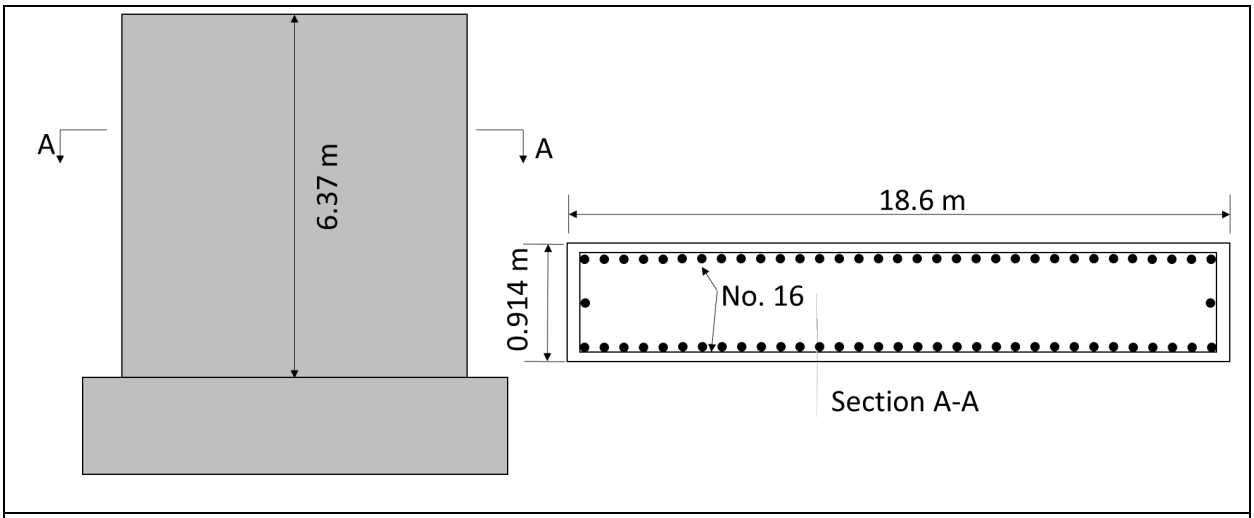

(g) Bridge NY-7

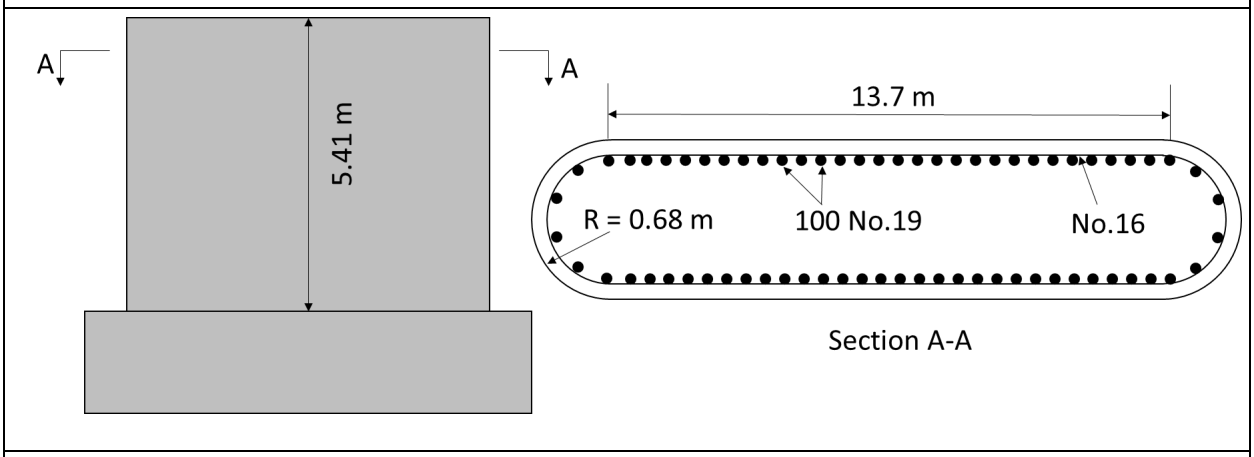

(h) Bridge NY-8

Figure 4: Layouts of NYSDOT bridge substructures

Table 3: Summary of WSDOT bridges

Bridge	Built year	Spans	Span length (m)		Superstructure		Substructure				
			Side	Middle	Deck type	Girder type	Substructure type	Rebar Size*		Concrete strength (MPa)	Rebar strength (MPa)
								Longitudinal	Transverse		
WS-1	1959	3	17.8	23.8	Concrete box	-	Columns	No.25	No.13	25	276
WS-2	1965	3	15.4	16.4	Concrete	Prestressed concrete	Columns	No.29	No.10	28	276
WS-3	1960	3	14.6	19.5	Voided concrete	-	Columns	No.29	No.13	25	276
WS-4	1960	4	10.7	19.3	Concrete	Prestressed concrete	Columns	No.32	No.10	25	276
WS-5	1963	3	16.3	16.3	Concrete	Prestressed concrete	Columns	No.29	No.10	28	276
WS-6	1966	3	14.8	17.5	Concrete	-	Columns	No.29	No.13	28	276
WS-7	1961	3	15.5	15.7	Concrete	Prestressed concrete	Columns	No.32	No.10	25	276
WS-8	1961	3	14.6	14.6	Concrete	Prestressed concrete	Columns	No.32	No.10	25	276

* The numbers indicate rebar diameter in mm.

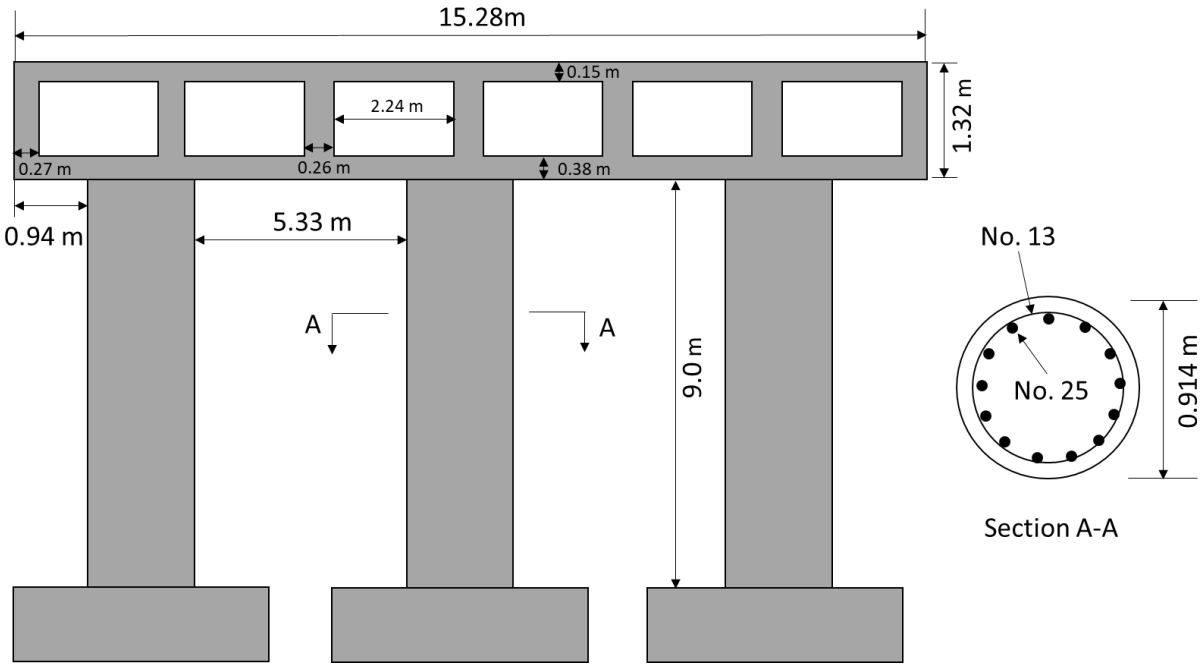

(a) Bridge WS-1

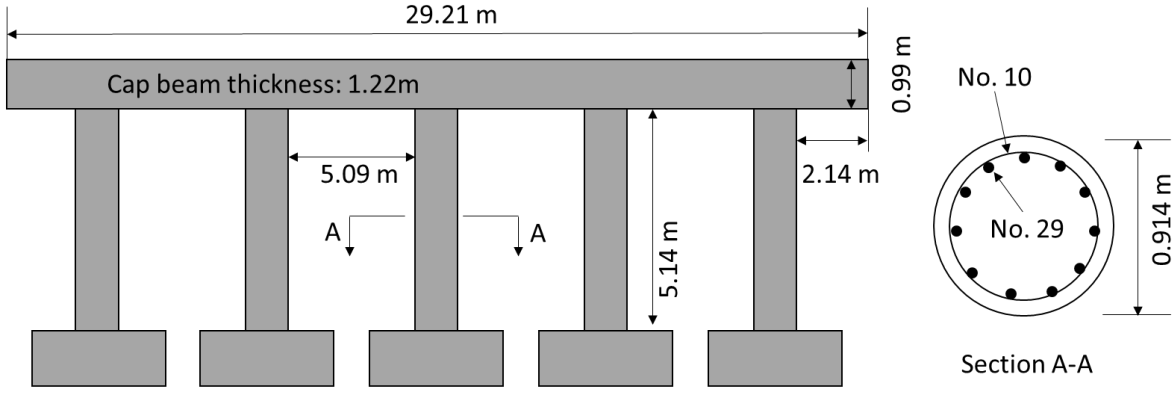

(b) Bridge WS-2

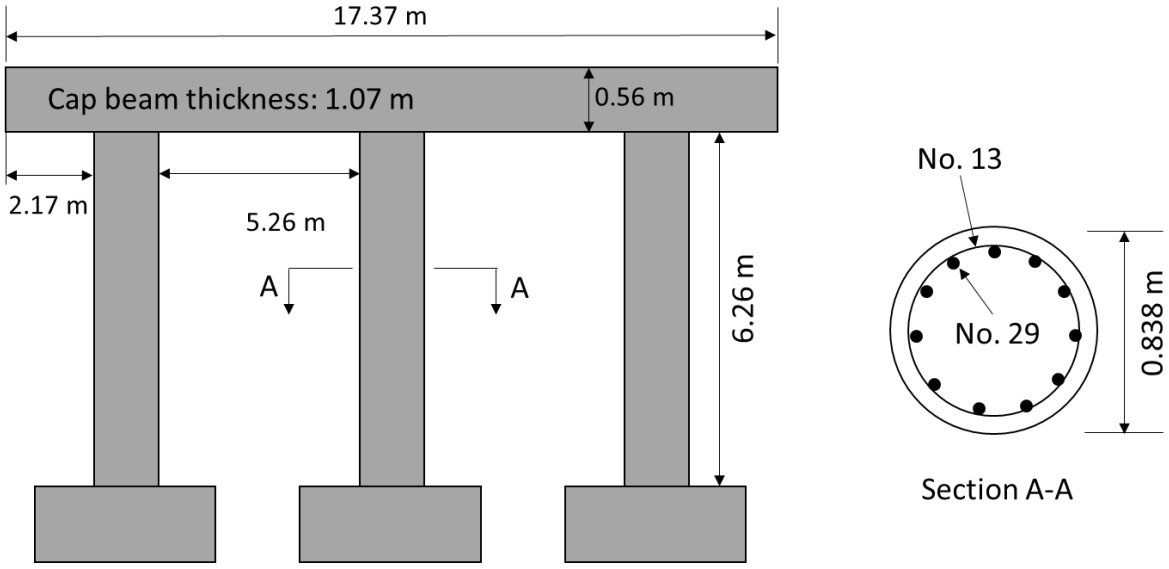

(c) Bridge WS-3

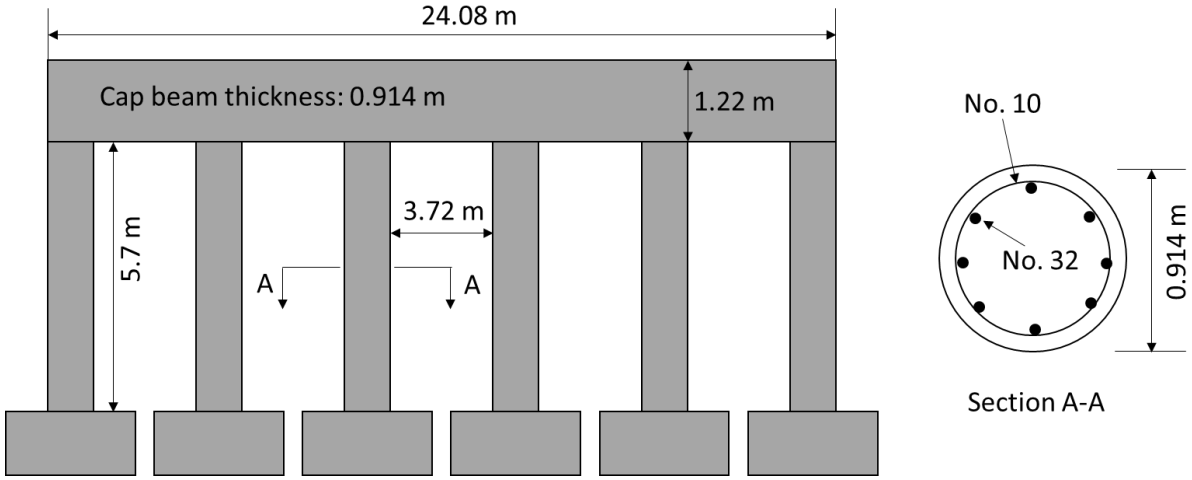

(d) Bridge WS-4

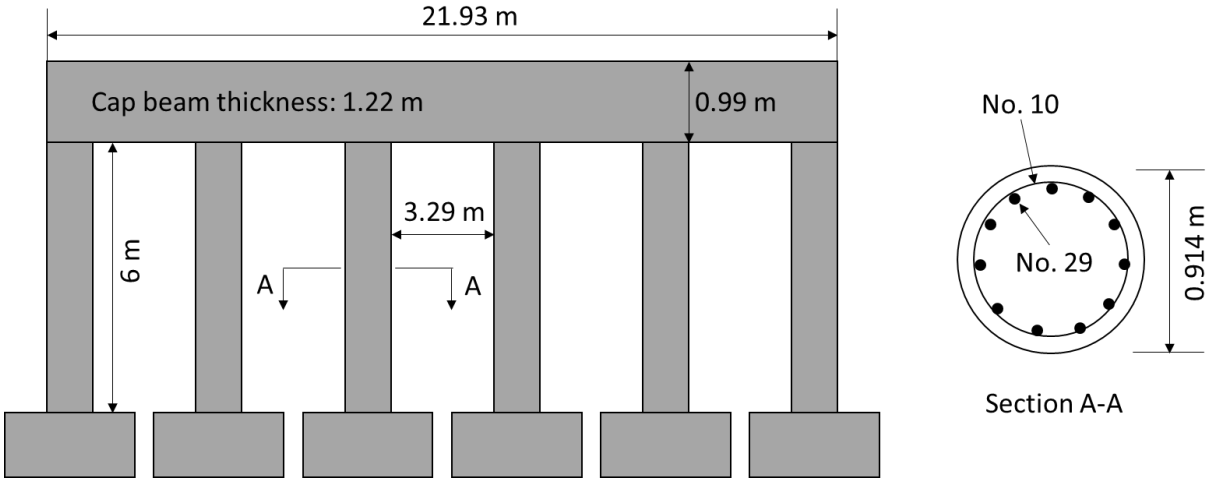

(e) Bridge WS-5

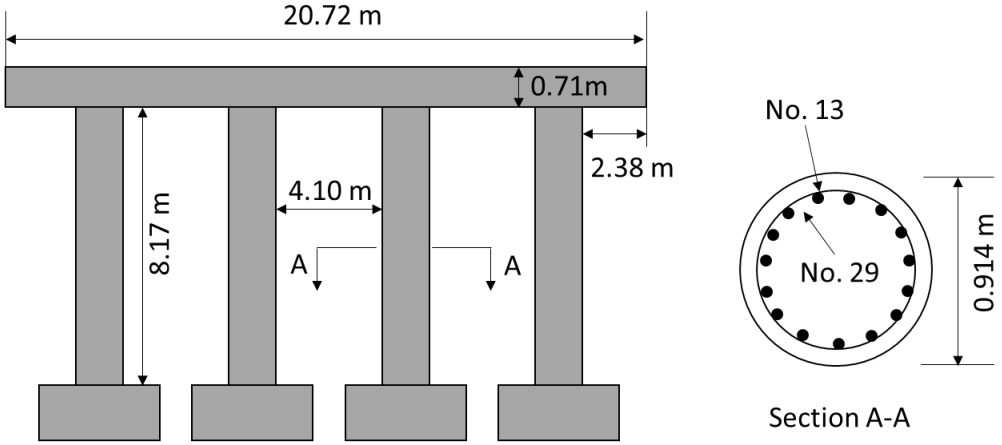

(f) Bridge WS-6

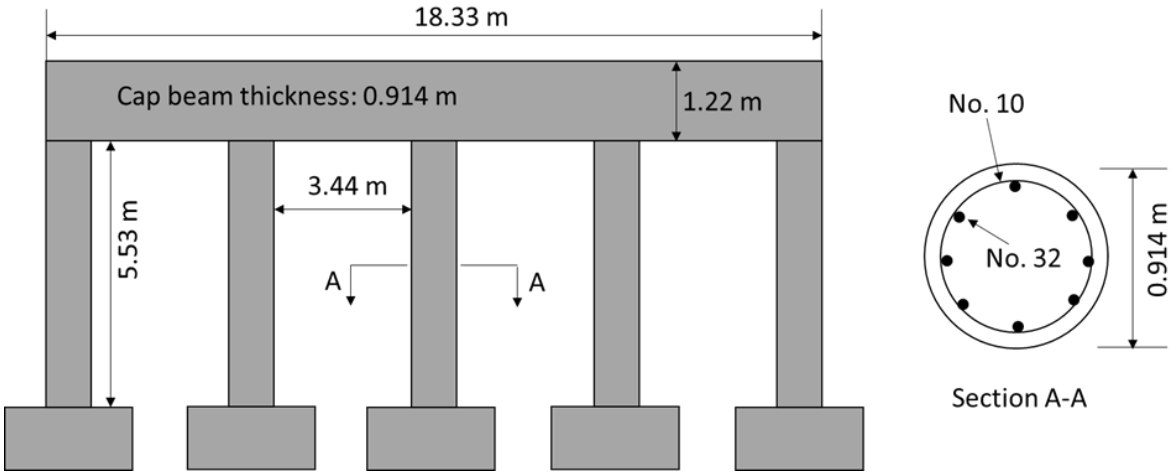

(g) Bridge WS-7

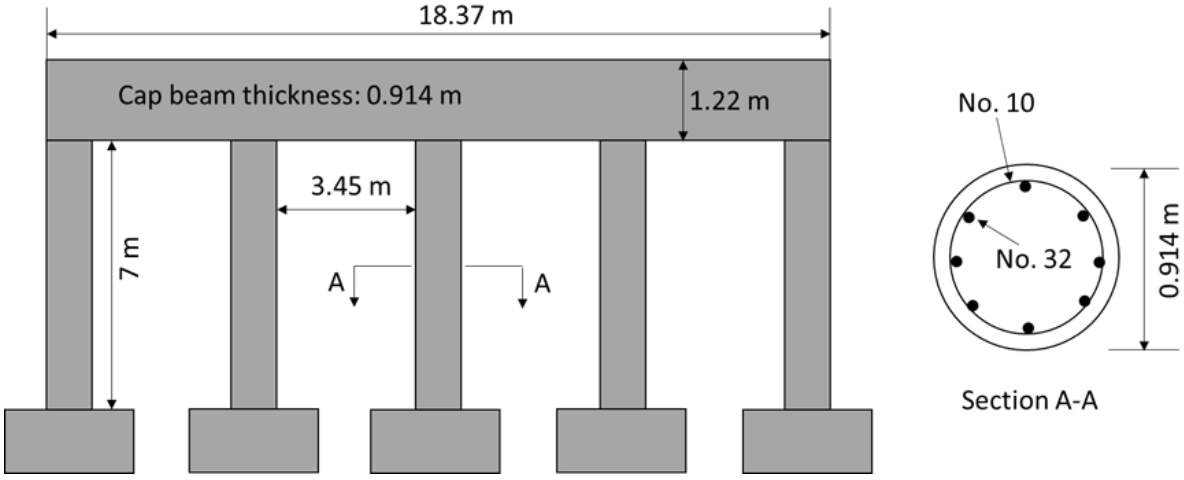

(h) Bridge WS-8

Figure 5: Layouts of WSDOT bridge substructures

5.2 Modeling strategies

The IDA used for the fragility analysis (Chapter 3) has a high computational cost, and it has to be performed multiple times for each bridge at different times across their lifespan. In order to improve the overall computational efficiency for a group of bridges, three assumptions were

made in this study: 1) the seismic performance of bridges was represented by the seismic performance of their substructures, with the rest of the bridge modeled as point masses and appropriate boundary conditions, 2) earthquake load was applied in the same direction as the traffic flow of the bridge, and 3) soil-structure interaction was not considered.

5.2.1 Finite element model

An open-source software, OpenSEES [33, 38, 41] was used to create a finite element model of each bridge pier, which was either a column (single or multiple columns) or a wall type, to generate the seismic fragility curves for various damage states. Each pier (column or wall) was modeled as a four-degree freedom system with a fixed base using a "displacement-based beam-column" element in OpenSEES. A fiber section was used to discretize the cross-section of a pier (column or wall). The important parts of the model for an example substructure are shown in Figure 6 (a). The model details of all the bridges investigated in this study are summarized in Table 4.

5.2.2 Material models

Unconfined concrete properties were assigned to the cover elements, whereas confined concrete properties, calculated by the model of Mander, Priestley [42], were assigned to the core elements. The stress-strain behavior of concrete was modeled using the Concrete07 material model in OpenSEES. This material model implements the concrete model by Chang and Mander [43] with simplified unloading and reloading curves, taking into account the tensile strength, descending portion of the compressive stress versus strain relation, and reduced stiffness during the unloading of concrete. After cover concrete attained the crack width of 1.0 mm, it was assumed

to be ineffective for carrying mechanical loads and was therefore removed from the dynamic structural analysis [44]. Reinforcing steel stress-strain behavior was modeled using the Steel02 material model in OpenSEES, which is based on the Giuffre-Menegotto-Pinto model [45], including isotropic strain hardening. The constitutive relationships of concrete07 and steel02 are shown in Figure 6 (c).

Table 4: Model details of bridges

Bridge name	Structure model	Height (m)	ρ_{long}	ρ_{trans}	P (KN)	P/(f'c×A)
NY-1	Column	3.80	1.1%	0.12%	2073.6	4.4%
NY-2	Wall	3.51	0.23%	0.17%	5850.4	3.1%
NY-3	Column	5.58	0.9%	0.20%	958.9	7.0%
NY-4	Wall	5.49	0.7%	0.26%	5403.6	1.7%
NY-5	Column	3.65	2.2%	0.48%	1689.9	5.7%
NY-6	Wall	4.40	0.08%	0.14%	4848.9	1.3%
NY-7	Wall	6.37	0.08%	0.17%	5430.8	1.5%
NY-8	Wall	5.41	0.14%	0.10%	4625.1	1.1%
WS-1	Column	9.00	1.0%	0.20%	3197.5	19%
WS-2	Column	5.14	1.1%	0.12%	1419.0	7.8%
WS-3	Column	6.26	1.3%	0.20%	1700.9	12.0%
WS-4	Column	5.70	0.9%	0.12%	1062.5	5.8%
WS-5	Column	6.00	1.1%	0.12%	908.5	5.0%
WS-6	Column	8.17	1.4%	0.20%	1615.9	8.9%
WS-7	Column	5.53	1.0%	0.12%	745.9	4.5%
WS-8	Column	7.00	1.0%	0.12%	715.5	4.4%

ρ_{long}: Longitudinal reinforcement ratio
ρ_{trans}: Transverse reinforcement ratio calcualted for different types of cross-sections per Mander, Priestley [42]
P: Superstructure weight
f'c: Compressive strength of unconfined concrete
A: Gross area of the cross-section

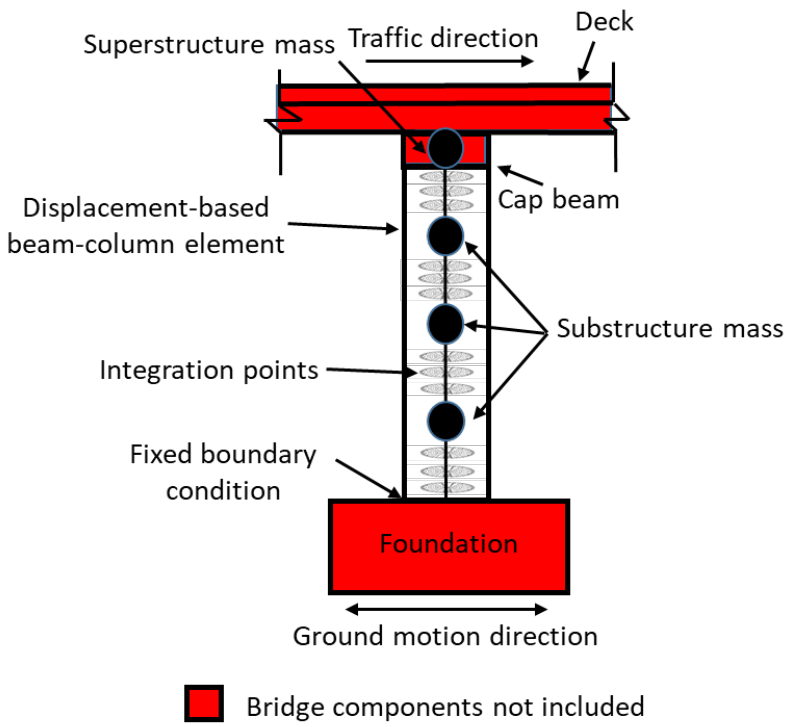

(a) Substructure model components

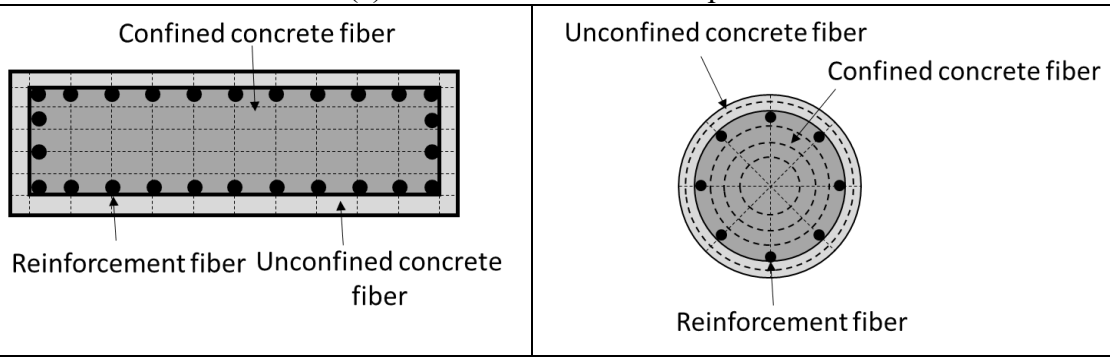

(b) Typical cross section

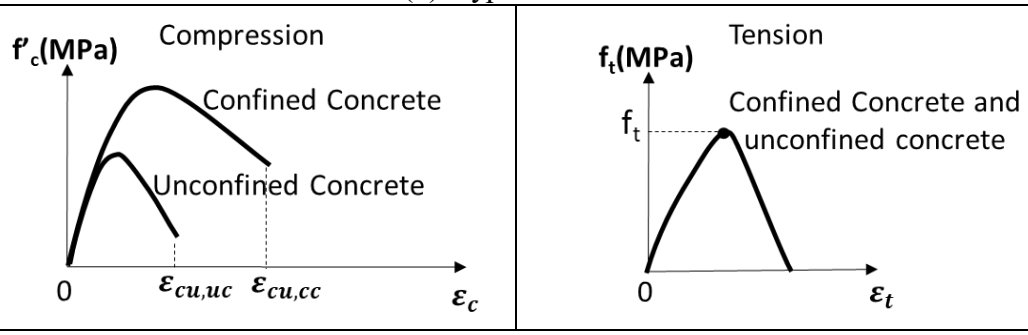

Concrete07 of OpenSEES material library

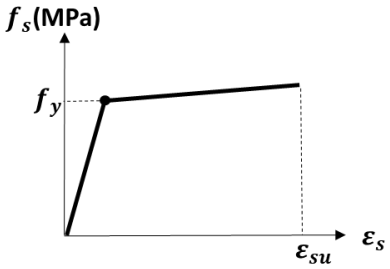

steel02 of OpenSEES material library

(c) Material properties

Figure 6: Model details

Chapter 6: Results and discussion

6.1 Corrosion model results

6.1.1 Corrosion initiation phase

The computed times to corrosion initiation for all the bridge substructures (columns/walls) are shown in Table 5. It should be noted that the surface chloride concentration and chloride diffusion coefficient for all the bridges of a state were assumed to be the same, as given in Section 2.3. Therefore, the difference in corrosion initiation times between the bridges of the same state was solely due to the difference in their concrete cover thicknesses. Larger cover thickness increases the distance between the external surface of the column/wall and the steel reinforcement, which in turn increases the time taken by the chloride ions to diffuse through the concrete cover. As observed in Table 5, the corrosion initiation time increases with increase in the concrete cover thickness. Additionally, the corrosion initiation time for the transverse reinforcement is shorter than that for the longitudinal reinforcement because the transverse reinforcement is closer to the exterior surface of a column/wall than the longitudinal reinforcement. A more refined prediction can be made if the local exposure conditions of each bridge, such as deicing salt amount on a specific road, are known and captured in corrosion modeling.

Among the NYSDOT bridges, NY-4 and NY-5 exhibited the longest and the shortest corrosion initiation times, respectively. Bridges NY-2 and NY-3 have the same corrosion initiation time for the transverse reinforcement, but NY-2 has a longer corrosion initiation time for longitudinal reinforcement than NY-3. This is because NY-2 has a larger size of transverse rebar

(No.16) compared to NY-3 (No.13), which slightly increases the distance of the longitudinal reinforcement from the external surface. Similarly, among the WSDOT bridges, WS-4 and WS-1 exhibited the longest corrosion initiation times for transverse and longitudinal reinforcement, respectively. Bridges WS-3 and WS-6 exhibited the shortest corrosion initiation time due to the smallest cover thickness.

Table 5: Corrosion initiation time

Bridge number	Cover thickness (mm)	Corrosion initiation time (years)	
		Longitudinal rebar	Transverse rebar
NY-1	47	9.0	6.0
NY-2	51	12.0	7.0
NY-3	51	10.0	7.0
NY-4	89	29.0	21.0
NY-5	35	7.0	3.0
NY-6	51	12.0	7.0
NY-7	51	12.0	7.0
NY-8	51	12.0	7.0
WS-1	57	20.0	13.0
WS-2	46	12.5	8.5
WS-3	38	10.5	6.0
WS-4	59	19.0	14.0
WS-5	46	12.5	8.5
WS-6	38	10.5	6.0
WS-7	46	12.5	8.5
WS-8	46	12.5	8.5

6.1.2 Corrosion propagation phase

As explained in Chapter 2, the rebar area reduces during the corrosion propagation phase. The calculated remaining rebar areas after 25, 50, and 75 years as percentages of the initial areas for all the bridges are shown in Table 6. In these calculations, corrosion is assumed to equally

reduce the area of all reinforcing bars. The results indicate that rebars with larger initial areas tend to exhibit slightly less percentage area reduction over time due to corrosion. For example, consider the longitudinal reinforcement bars in bridges WS-2 and WS-7. Although the corrosion initiation times for both the bridges are the same, the remaining rebar area in WS-7 (with No.32 longitudinal rebars) after 75 years is 2.5% larger than that WS-2 (with No.29 longitudinal rebars). Pitting corrosion considered in this study causes the same absolute rebar area reduction regardless of the bar size, which in turn lowers the percentage area reduction for larger bar sizes. NYSDOT bridges NY-6 and NY-7 and WSDOT bridges WS-3 and WS-4 exhibit the least remaining longitudinal reinforcement areas after 75 years in their respective groups, which makes them the most vulnerable to seismic damage as shown in the following sections.

Table 6: Remaining rebar area

Bridge number	Remaining rebar area (%)					
	After 25 years		After 50 years		After 75 years	
	Long.	Trans.	Long.	Trans.	Long.	Trans.
NY-1	99.7	96.3	96.3	72.0	89.1	34.7
NY-2	99.4	98.0	90.6	82.3	72.2	55.6
NY-3	99.6	96.8	94.4	73.0	83.2	36.0
NY-4	99.8	98.0	96.8	93.0	89.8	72.0
NY-5	99.7	96.6	96.5	78.9	90.0	51.1
NY-6	99.2	98.0	86.5	82.3	61.5	55.6
NY-7	99.2	98.0	86.5	82.3	61.5	55.6
NY-8	99.5	98.0	90.6	82.3	72.2	55.6
WS-1	99.9	99.0	97.0	81.0	87.9	46.0
WS-2	99.8	95.6	96.1	58.4	87.5	8.9
WS-3	99.7	96.2	95.5	71.7	86.5	34.4
WS-4	99.9	98.5	98.1	68.8	92.2	18.6
WS-5	99.8	95.6	96.1	58.5	87.5	8.9
WS-6	99.7	96.2	95.5	71.7	86.5	34.4
WS-7	99.8	95.6	96.9	58.5	90.0	8.9
WS-8	99.8	95.6	96.9	58.5	90.0	8.9

Long.: Longitudinal rebar
Trans.: Transverse rebar

6.2 Seismic damage probability

Figure 7 shows the damage probability variation over 75 years (since the built year) for NYSDOT bridges at all the damage states. The damage probabilities for all the bridges are low (less than 0.03%) due to the low seismicity in New York State. For every bridge, the damage probability increases over time due to corrosion. For example, the probability of extensive damage for bridge NY-1 increases by approximately 25% after 75 years relative to the as-built condition. Bridges with multi-column piers are more fragile than bridges with pier wall, which is due to the larger stiffness of the pier wall, reducing the dynamic responses.

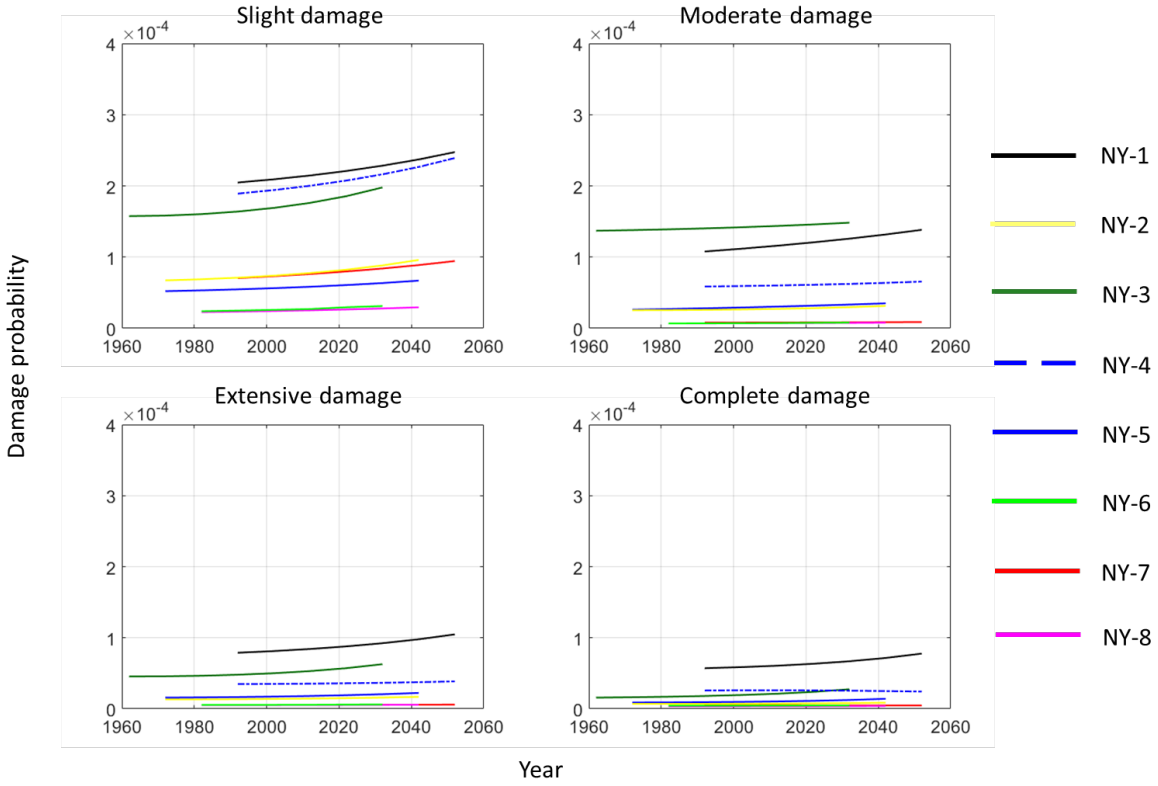

Figure 7: Damage probability for bridges from NYSDOT

Figure 8 shows the damage probability variation over 75 years (since the built year) for WSDOT bridges at all the damage states. Compared to the NYSDOT bridges, the damage probabilities of WSDOT bridges are approximately two orders of magnitude larger at all the damage states due to high seismicity in Washington State. For the slight damage state, which is marked by the onset of yielding in the outermost longitudinal rebar, the damage probability is mainly controlled by the height and the axial load ratio [$P/(f'_c \times A)$] (given in Table 4) of the bridge substructures. The tallest WSDOT bridge substructures, WS-1, WS-6, and WS-8, exhibit the lowest probabilities of slight damage. This is because the bridge substructures with larger heights have smaller stiffness, which increases the displacement causing yielding in the outermost rebar. Although the low stiffness also increases the dynamic responses of the bridge column, the yielding of rebar happens under low seismic force. Therefore, the increase in the dynamic response is not as significant as the increase in the displacement for the yielding of the rebar, which results in a low probability of damage at slight damage states. For bridge WS-7, although it is not as tall as WS-1, WS-6, and WS-8, the probability of slight damage is low because the axial load ratio of WS-7 is much lower than other bridges, resulting in the smaller seismic force (inertial force) and smaller responses in dynamic analysis.

The damage probability is mainly controlled by the axial load ratio [$P/(f'_c \times A)$] at moderate and extensive damage states. As a result, bridges WS-1, WS-2, WS-3, and WS-6, which have the largest axial load ratios, exhibit the largest probabilities of moderate and extensive damage among the WSDOT bridges. This is because the large axial load ratio results in the larger seismic force (inertial force), which increases the dynamic responses.

For the complete damage state, which is marked by achieving the ultimate strain in confined concrete (calculated by equation 17 in Chapter 3), the damage probability is mainly affected by the axial load ratio and transverse reinforcement ratio of the bridge substructures (given in Table 4). The bridges that exhibited the highest damage probability are WS-1, WS-2, and WS-3. These bridges have the highest axial load ratio. As mentioned before, a large axial load ratio results in a large seismic force. The bridge WS-6 has a larger axial load ratio than WS-2. However, its probability of damage is lower because the WS-6 has a larger transverse reinforcement ratio, which increases the ultimate strain in confined concrete, resulting in a more ductile performance.

It is interesting to note that at moderate and extensive damage states, the damage probability of bridge WS-4 increases the fastest among all bridges over time. This is because WS-4 has the smallest concrete core left after 50 years. All the concrete cover is assumed to have spalled when the crack width (due to corrosion damage) reached 1 mm (Section 5.2.2). All the WSDOT bridge columns have the same gross section area (including cover). Therefore, after cover removal due to corrosion damage, WS-Bridge 4 has the smallest residual section area (as it has the largest cover thickness, as shown in Table 5), which resulted in the largest decrease in stiffness and the largest increase in dynamic responses.

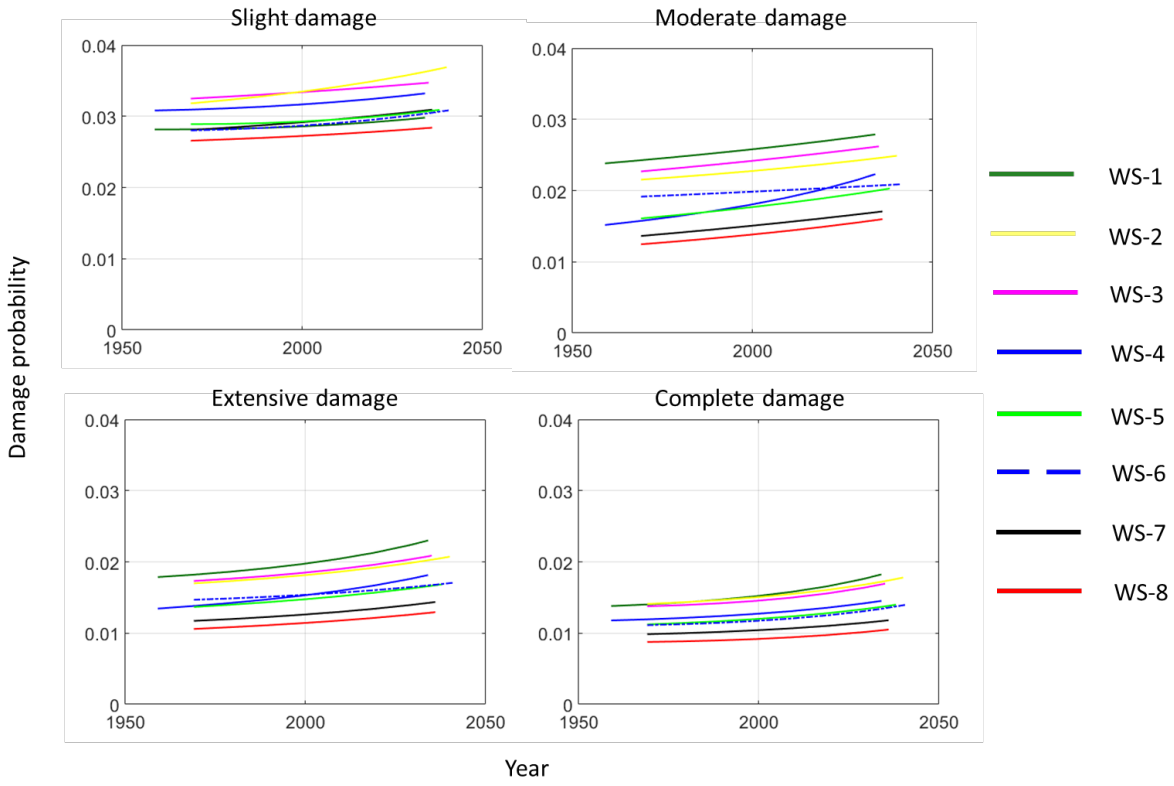

Figure 8: Damage probability for bridges from WSDOT

When evaluating their inventory, departments of transportation are anticipated to assign a higher priority of maintenance, repair and retorif to bridges that have the highest expected damage probability per Figure 7 and 8. For both New York and Washington State bridges, the order of damage probability (and therefore priority of intervening actions) of bridges in the group changed over time for some damage states, as suggested by damage probability curves crossing one another in Figures 7 and 8. This indicates that departments of transportation that do not consider deterioration in their seismic damage assessment may not be able to correctly identify bridges with the highest risk of seismic damage. It should be noted that the bridges selected for this study for demonstration of the assessment were built in similar years. In addition, the corrosion model captured the general environmental conditions in a state, but did not consider local exposure conditions for each individual bridge. For bridges with large differences in age and local exposure

conditions, the order of seismic damage risk is expected to change more drastically than the bridges considered in this study for the demonstration of the assessment method.

Chapter 7: Conclusions

This report demostrates the application of a systematic framework for determining the seismic vulnerability of a group of bridges undergoing corrosion deterioration. Two groups of bridges, one owned by the New York State Department of Transportation (NYSDOT) and the other owned by Washington State Department of Transportation (WSDOT), were considered in this project. The computational framework consists of three parts: corrosion modeling, seismic fragility analysis, and risk analysis. The framework takes into account the effects of several key parameters on the corrosion and structural models. Most importantly, the effects of pitting corrosion on both longitudinal and transverse reinforcement areas, the effects of cracking in concrete cover on corrosion rates, and the effects of site-specific seismic hazard curves are considered in this framework. The main conclusions of this research are given below:

1. All bridges become more vulnerable to seismicity due to corrosion deterioration. Therefore, neglecting the effects of corrosion deterioration may lead to unconservative estimates of seismic damage risk. Seismic evaluation of bridges should be performed considering the current state of bridge substructures, as documented by inspections (if available) or as predicted by a corrosion model such as the one presented in this study. For planning future repair and retrofit actions, the combined seismic and corrosion model presented in this study can be used to predict the performance of bridges in an inventory considering both hazards, allowing prioritization of intervening actions as well as quantification of the impacts of these actions on bridge performance.

2. The demonstration of application of the seismic and corrosion assessment of bridges using a group of bridges showed that that the order of seismic vulnerability of bridges in an inventory can change over time due to corrosion. This implies that departments of transportation that do not consider corrosion in seismic assessments may not be able to identify bridges with the highest need of maintenance, repair or retrofit. The effect of corrosion on the order of seismic damage probability of bridges in a group is expected to be more significant for inventories with a large variability in bridge age, bridge characteristics and local exposure condition.

3. The order of seismic damage vulnerability did not change for some bridges. This may be due to the assumption of similar local conditions (such as salt exposure), and similar ages for some bridges. Incorporation of effects of local exposure conditions into the corrosion model may refine the results presented in this report.

This project demonstrated the use of the framework on a small group of pilot bridges, to aid in implementation of the framework by departments of transportation to larger bridge inventories. In this project, the framework was used to evaluate bridges under the combined seismic hazard and corrosion, to quantify seismic damage probability along service life, to identify bridges in a network with a higher damage risk, and therefore, to inform maintenance decisions for a group of bridges. The assessment can also be used to quantify the return-on-investment for new materials, design methods, and construction practices.

References

1. Basöz, N.I., et al., *Statistical analysis of bridge damage data from the 1994 Northridge, CA, earthquake.* Earthquake spectra, 1999. **15**(1): p. 25-54.
2. Grossi, P., *Catastrophe modeling: a new approach to managing risk*. Vol. 25. 2005. Berlin: Springer Science & Business Media.
3. Bommer, J., et al., *Development of an earthquake loss model for Turkish catastrophe insurance.* Journal of Seismology, 2002. **6**(3): p. 431-446.
4. Koch, G.H., et al., *Corrosion cost and preventive strategies in the United States*. 2002. Washington, D.C., U.S.
5. ASCE. *2017 infrastructure report card*. 2017 [cited 2020 May 20]; Available from: https://www.infrastructurereportcard.org.
6. Choe, D.-E., et al., *Seismic fragility estimates for reinforced concrete bridges subject to corrosion.* Structural Safety, 2009. **31**(4): p. 275-283.
7. Choe, D.-E., et al., *Probabilistic capacity models and seismic fragility estimates for RC columns subject to corrosion.* Reliability Engineering & System Safety, 2008. **93**(3): p. 383-393.
8. Alipour, A., B. Shafei, and M. Shinozuka, *Performance evaluation of deteriorating highway bridges located in high seismic areas.* Journal of Bridge Engineering, 2010. **16**(5): p. 597-611.
9. Akiyama, M., D.M. Frangopol, and H. Matsuzaki, *Life-cycle reliability of RC bridge piers under seismic and airborne chloride hazards.* Earthquake Engineering & Structural Dynamics, 2011. **40**(15): p. 1671-1687.

10. Biondini, F., E. Camnasio, and A. Palermo, *Lifetime seismic performance of concrete bridges exposed to corrosion.* Structure and Infrastructure Engineering, 2014. **10**(7): p. 880-900.

11. Ghosh, J. and J.E. Padgett, *Aging considerations in the development of time-dependent seismic fragility curves.* Journal of Structural Engineering, 2010. **136**(12): p. 1497-1511.

12. Afsar Dizaj, E., R. Madandoust, and M.M. Kashani, *Exploring the impact of chloride-induced corrosion on seismic damage limit states and residual capacity of reinforced concrete structures.* Structure and Infrastructure Engineering, 2018. **14**(6): p. 714-729.

13. Zhang, Y., R. DesRoches, and I. Tien, *Impact of corrosion on risk assessment of shear-critical and short lap-spliced bridges.* Engineering Structures, 2019. **189**: p. 260-271.

14. Ghosh, J. and P. Sood, *Consideration of time-evolving capacity distributions and improved degradation models for seismic fragility assessment of aging highway bridges.* Reliability Engineering & System Safety, 2016. **154**: p. 197-218.

15. Cui, F., et al., *Seismic fragility analysis of deteriorating RC bridge substructures subject to marine chloride-induced corrosion.* Engineering Structures, 2018. **155**: p. 61-72.

16. Stewart, M.G. and A. Al-Harthy, *Pitting corrosion and structural reliability of corroding RC structures: Experimental data and probabilistic analysis.* Reliability engineering & system safety, 2008. **93**(3): p. 373-382.

17. Darmawan, M., *Pitting corrosion model for reinforced concrete structures in a chloride environment.* Magazine of Concrete Research, 2010. **62**(2): p. 91.

18. Otieno, M., M. Alexander, and H.-D. Beushausen, *Corrosion in cracked and uncracked concrete–influence of crack width, concrete quality and crack reopening.* Magazine of Concrete Research, 2010. **62**(6): p. 393-404.

19. Cao, C., M.M. Cheung, and B.Y. Chan, *Modelling of interaction between corrosion-induced concrete cover crack and steel corrosion rate.* Corrosion Science, 2013. **69**: p. 97-109.

20. Simon, J., M. Bracci Joseph, and P. Gardoni, *Seismic Response and Fragility of Deteriorated Reinforced Concrete Bridges.* ASCE Journal of Structural Engineering, 2010. **136**(10): p. 1273-1281.

21. Crank, J., *The mathematics of diffusion*. 1979, New York: Oxford University Press Inc.

22. Bertolini, L., et al., *Corrosion of steel in concrete: prevention, diagnosis, repair*. Vol. 392. 2004, Weinheim: WILEY-VCH Verlag GmbH & Co. KGaA.

23. Val, D.V. and R.E. Melchers, *Reliability of deteriorating RC slab bridges.* Journal of structural engineering, 1997. **123**(12): p. 1638-1644.

24. Du, Y., L. Clark, and A. Chan, *Residual capacity of corroded reinforcing bars.* Magazine of Concrete Research, 2005. **57**(3): p. 135-147.

25. El Maaddawy, T. and K. Soudki, *A model for prediction of time from corrosion initiation to corrosion cracking.* Cement and concrete composites, 2007. **29**(3): p. 168-175.

26. Vidal, T., A. Castel, and R. Francois, *Analyzing crack width to predict corrosion in reinforced concrete.* Cement and concrete research, 2004. **34**(1): p. 165-174.

27. Yuan, Y., J. Jiang, and T. Peng, *Corrosion process of steel bar in concrete in full lifetime.* ACI Materials Journal, 2010. **107**(6): p. 562.

28. Weyers, R.E., et al., *Concrete Bridge Protection and Rehabilitation: Chemical and Physical Techniques. Service Life Estimates*. 1994. Washington, D.C., U.S.

29. Enright, M.P. and D.M. Frangopol, *Probabilistic analysis of resistance degradation of reinforced concrete bridge beams under corrosion.* Engineering structures, 1998. **20**(11): p. 960-971.

30. Life-365™. *Life-365 service life predication model™*. 2013 [cited 2020 Sep. 9]; Available from: http://www.life-365.org.

31. Andrade, C. and C. Alonso, *On-site measurements of corrosion rate of reinforcements.* Construction and building materials, 2001. **15**(2-3): p. 141-145.

32. ATC, *Quantification of building seismic performance factors*. 2009. Federal Emergency Management Agency, Washington, D.C.

33. McKenna, F., G.L. Fenves, and M.H. Scott. *Open system for earthquake engineering simulation*. 2000 [cited 2020 Sep. 1]; Available from: http://opensees.berkeley.edu.

34. Vamvatsikos, D. and C.A. Cornell, *Incremental dynamic analysis.* Earthquake Engineering & Structural Dynamics, 2002. **31**(3): p. 491-514.

35. Paulay, T. and M.N. Priestley, *Seismic design of reinforced concrete and masonry buildings*. 1992, New York: John Wiley & Sons, Inc.

36. Nielson, B.G. and R. DesRoches, *Seismic fragility methodology for highway bridges using a component level approach.* Earthquake Engineering & Structural Dynamics, 2007. **36**(6): p. 823-839.

37. Baker, J.W., *Efficient analytical fragility function fitting using dynamic structural analysis.* Earthquake Spectra, 2015. **31**(1): p. 579-599.

38. USGS. *Earthquake Hazards*. 2020 [cited 2020 Oct. 10]; Available from: https://www.usgs.gov/natural-hazards/earthquake-hazards/earthquakes.

39. McGuire, R.K., *Probabilistic seismic hazard analysis: Early history.* Earthquake Engineering & Structural Dynamics, 2008. **37**(3): p. 329-338.

40. ASCE, *Seismic design criteria for structure s, systms, and components in nuclear facilities*. 2005: Reston, VA.

41. Mazzoni, S., et al., *OpenSees command language manual.* Pacific Earthquake Engineering Research (PEER) Center, 2006. California, U.S.

42. Mander, J.B., M.J. Priestley, and R. Park, *Theoretical stress-strain model for confined concrete.* Journal of structural engineering, 1988. **114**(8): p. 1804-1826.

43. Chang, G. and J.B. Mander, *Seismic energy based fatigue damage analysis of bridge columns: part 1-evaluation of seismic capacity*. 1994. New York, U.S.

44. Cheng, H., et al., *Seismic fragility analysis of deteriorating RC bridge columns with time-variant capacity index.* Bulletin of Earthquake Engineering, 2019: p. 1-21.

45. Filippou, F.C., V.V. Bertero, and E.P. Popov, *Effects of bond deterioration on hysteretic behavior of reinforced concrete joints*. 1983, Earthquake Engineering Research Center, California, U.S.